

Black hole masses and starbursts in X-shaped radio sources

M. Mezcua¹ *, A.P. Lobanov¹, V.H. Chavushyan², and J. León-Tavares^{1,2,3}

¹ Max Planck Institute for Radio Astronomy, Auf dem Hügel 69, 53121 Bonn

² Instituto Nacional de Astrofísica, Óptica y Electrónica, Apdo. Postal 51, 72000 Puebla, México

³ Aalto University Metsähovi Radio Observatory, Metsähovintie 114, FIN-02540 Kylmälä, Finland

Preprint online version: December 4, 2018

ABSTRACT

It has been suggested that the X-shaped morphology observed in some radio sources can reflect either a recent merger of two supermassive black holes (SMBHs) or the presence of a second active black hole in the galactic nucleus. These scenarios are tested by studying the relationship between the black hole mass, radio and optical luminosity, starburst history, and dynamic age of radio lobes in a sample of 29 X-shaped radio galaxies drawn from a list of 100 X-shaped radio source candidates identified from the FIRST survey. The same relationships are also studied in a control sample consisting of 36 radio-loud active nuclei with similar redshifts and optical and radio luminosities. The X-shaped objects are found to have statistically higher black hole masses and older starburst activity compared with the objects from the control sample. Implications of these findings are discussed for the black hole merger scenario and for the potential presence of active secondary black holes in post-merger galaxies.

Key words. Galaxies: kinematics and dynamics – Galaxies: formation – Galaxies: nuclei – Black hole physics

1. Introduction

X-shaped (or ‘winged’) radio galaxies are a class of extragalactic radio sources with two low-surface-brightness radio lobes (the ‘wings’) oriented at an angle to the active, or high-surface-brightness, lobes (Leahy & Williams 1984). Both sets of lobes often pass symmetrically through the center of the host galaxy, giving the galaxy an X-shaped morphology as seen on radio maps. Several authors have attempted to explain the unusual structure in X-shaped sources. Rees (1978) suggested that the X-shaped morphology may result from a precession of the jet caused by misalignment between the angular momenta of the central supermassive black hole (SMBH) and the gas accreted onto it. Subsequently, four different scenarios were proposed for the formation of this peculiar radio morphology: 1) backflow from the active lobes into the wings (Leahy & Williams 1984; Capetti et al. 2002); 2) slow conical precession of the jet axis (Parma, Ekers & Fanti 1985; Mack et al. 1994); 3) reorientation of the jet axis during which flow continues; and 4) reorientation of the jet axis, but the jet turned off or at greatly reduced power during the change of direction (Dennett-Thorpe et al. 2002). Merritt & Ekers (2002) suggested that the reorientation of a black hole spin axis owing to a minor merger may lead to a sudden flip in the direction of the associated jet. In this

case, X-shaped galaxies would be the sites of spin-flips associated with recent coalescences of pairs of supermassive black holes (Gopal-Krishna et al. 2003; Gergely & Biermann 2009). The older wings would then represent relics of past radio jets, while the active lobes would reflect the activity that ensued after the black hole merger. Hence, synchrotron aging should lead to a steeper spectral index in the wings or low-surface brightness features than in the high-surface brightness active lobes. However, in some X-shaped sources, the wings have a similar or even flatter spectral index than the active lobes (Lal & Rao 2005). To explain this discrepancy Lal & Rao (2005) suggested that at least some of the X-shaped sources may contain coalescing binary SMBH systems with two pairs of jets associated with two unresolved AGN. The activity of the secondary black holes in post-merger galaxies is suggested to depend on the separation and mass ratio of the two SMBH (Lobanov 2008), with equal mass mergers providing the longest time during which both SMBH remain active, while minor mergers lead to rapid disruption of the accretion disks around the secondary black hole and to quench of its activity (the primary black hole in minor merger systems may however remain active for a much longer time compared with the activity duration in equal mass mergers, *cf.*, Dokuchaev 1991)

Several studies have been carried out in the optical and X-ray band, with results in some cases favoring the hydrodynamic backflow model over the merger-induced rapid reorientation sce-

* Email:mmezcua@mpifr.de

Member of the International Max Planck Research School (IMPRS) for Astronomy and Astrophysics at the Universities of Bonn and Cologne.

nario (*e.g.*, Hodges-Kluck et al. 2010; Landt et al. 2010), and in other cases favoring the merger model as the best explanation for the observed winged morphology (Hodges-Kluck et al. 2010b). A more detailed review of the different scenarios proposed to explain the origin of X-shaped radio galaxies is presented by Gopal-Krishna et al. (2010).

In all schemes in which X-shaped objects are the product of galactic mergers, the properties of the nuclear region will be affected by the past SMBH merger or the presence of a secondary SMBH. This should then be reflected by statistically higher masses of the central black holes in galaxies hosting the X-shaped radio. If the X-shaped morphology is indeed caused by a profound event in the nuclear region, such as a merger of two SMBH, then it may also be reflected in the starburst history of the host galaxy (Blecha et al. 2010). Investigations of the black hole masses and starburst histories can therefore address the question of the physical nature of the X-shaped sources and their difference from the “canonical” radio galaxies, if representative samples of both radio types are studied and compared against each other.

In this paper, we determine the black hole masses, luminosities, starburst histories, and jet dynamic ages in a sample of X-shaped galaxies and compare them with a control sample of radio-loud active nuclei with similar redshifts and optical and radio luminosities.

The target and control samples used for the study are introduced in Sect. 2. Section 3 describes the data analysis and methods employed for determination of the black hole masses and dynamic ages of the radio emission. Results of these measurements are presented in Sect. 4. A discussion of the results and their broader implication is given in Sect. 5.

Throughout this paper, we assume a Λ -CDM cosmology with parameters $H_0 = 73 \text{ km s}^{-1} \text{ Mpc}^{-1}$, $\Omega_\Lambda = 0.73$ and $\Omega_m = 0.27$.

2. The sample

The sample of AGN analyzed here is drawn from a list of known X-shaped sources and a list of 100 ‘winged’ and X-shaped radio source candidates (Cheung 2007) that were morphologically identified in the images from the VLA FIRST survey (Becker et al. 1995).

Of the 100 X-shaped candidates, 22 were found to have spectroscopic information in the Sloan Digital Sky Survey (SDSS) data release (DR6; Adelman-McCarthy et al. 2008), and optical spectra for additional 27 objects were obtained by Cheung et al. (2009) with the 9.2 m Hobby-Eberly Telescope (HET) at McDonald Observatory and the 6.5 m Multiple-Mirror Telescope (MMT) at Mt. Hopkins Observatory.

Cheung et al. (2009) have defined a subsample of 50 radio galaxies with bona fide X-shaped radio morphology. Because

this selection was based on visual inspection of the candidate objects and lacks quantifiable selection criteria, we refer to the original sample of Cheung (2007) for selecting appropriate candidates for our study. We select the X-shaped objects with optical spectra that show well-detected stellar absorption lines. Our final sample comprises 18 X-shaped radio sources with SDSS spectra complemented by five of the 27 X-shaped objects with spectra presented in Cheung et al. (2009), and six of the previously known X-shaped radio sources: 3C192, 4C+32.25, 4C+48.29 and 1059+169 (Lal & Rao 2007), 3C223.1 (Lal & Rao 2005) and 4C+01.30 (Wang et al. 2003) with spectra also available in the SDSS.

In order to evaluate the results obtained for the X-shaped radio galaxies, we compile a control sample of 19 radio-loud sources from Marchesini et al. (2004) plus 6 Fanaroff-Riley type II (FR II) sources from de Vries et al. (2006), and 11 radio loud elliptical galaxies from González-Serrano & Carballo (2000) that have SDSS spectra, and cover the same ranges of redshift ($z < 0.3$) and optical and radio luminosities as the objects in the target sample. The resulting common luminosity ranges for both samples are: $\log \lambda L_{5100\text{\AA}} \in [43.0, 46.0]$ and $\log \nu L_{1.4\text{GHz}} \in [39.0, 44.5]$. According to the Kolmogorov-Smirnov test (KS-test) the two samples differ at 0.9σ , which warrants making statistical comparisons between them.

3. Data analysis

The optical spectra of the objects in both samples have been used to measure properties of $H\beta$ and [OIII] emission lines and a number of stellar absorption lines. These measurements were applied to making kinematic mass estimates of the central black holes. The absorption line fits were also used to recover starburst histories in the host galaxies and to estimate the epochs of the most recent starburst. Angular sizes of active lobes and inactive wings (in X-shaped objects) were measured to determine the dynamic ages of the radio emission in the X-shaped objects and in the objects from the control sample.

3.1. Stellar absorption lines

The SDSS spectra collected for the objects in both samples contain several significant stellar absorption features (such as Ca H+K $\lambda\lambda 3969, 3934$, the Mg I b $\lambda\lambda 5167, 5173, 5184$ triplet, and the Ca II $\lambda\lambda 8498, 8542, 8662$ triplet, etc.) that can be matched against a combination of different synthetic stellar template spectra, yielding an estimate of the stellar velocity dispersion.

We use the stellar population synthesis code STARLIGHT (Asari et al. 2007; Cid Fernandes et al. 2004, 2005, 2007; Mateus et al. 2006) to model the observed spectrum O_λ . The best fit is obtained using a linear combination of simple stellar populations (SSPs) from the stellar library of Bruzual & Charlot (2003) and

a power-law component representing the AGN continuum emission. In our fitting, we apply the standard stellar library consisting of 150 SSPs, and complement the fit with up to six power-law components given by $F(\lambda) = 10^{20}(\lambda/4020)^\beta$, where $\beta = -0.5, -1, -1.5, -2, -2.5, -3$. Each SSP spans across six metallicities, $Z = 0.005, 0.02, 0.2, 0.4, 1, \text{ and } 2.5 Z_\odot$, with 25 different ages between 1 Myr and 18 Gyr. The Galactic extinction caused by the foreground dust screen is modeled and parametrized by the V-band extinction, A_V . We adopt the extinction law of Cardelli et al. (1989).

The resulting model spectrum M_λ (combining an SSP and a power-law continuum components) is

$$M_\lambda(x, M_{\lambda_0}, A_V, v_*, \sigma_*) = M_{\lambda_0} \left[\sum_{j=1}^{N_*} x_j b_{j,\lambda} r_\lambda \right] \otimes G(v_*, \sigma_*), \quad (1)$$

where $b_{j,\lambda} \equiv L_\lambda^{SSP}(t_j, Z_j)/L_{\lambda_0}^{SSP}(t_j, Z_j)$ is the j^{th} template normalized at λ_0 , x is the population vector, M_{λ_0} is the synthetic flux at the normalization wavelength, $r_\lambda \equiv 10^{-0.4(A_\lambda - A_{\lambda_0})}$ is the reddening term, and $G(v_*, \sigma_*)$ is the line-of-sight stellar velocity distribution, modeled as a Gaussian feature centered at velocity v_* and broadened by σ_* . The best fit is reached by minimizing χ^2 ,

$$\chi^2(x, M_{\lambda_0}, A_V, v_*, \sigma_*) = \sum_{\lambda=1}^{N_\lambda} [(O_\lambda - M_\lambda)w_\lambda]^2, \quad (2)$$

where the weighted spectrum w_λ is defined as the inverse of the noise in the observed spectra. A more detailed description of the STARLIGHT code and its applications can be found in Asari et al. (2007); Cid Fernandes et al. (2004, 2005, 2007); Mateus et al. (2006); Leon-Tavares et al. (2010).

The fit for the X-shaped source J1424+2637 is shown as an example in Fig. 1. The observed spectrum is shown in black, the host galaxy model in red, and the AGN power-law continuum in blue. The residual spectrum obtained after the subtraction of the stellar light and the continuum is shown in green.

In order to assess the fidelity of the STARLIGHT fit, we introduce a quality factor Q that combines the reduced χ^2 parameter of the modeled spectra, the velocity dispersion, σ_* , and its error, δ_* : $Q = (\chi^2 \delta_* / \sigma_*)^{-1/2}$. Fits with $Q > 10$ can be considered reliable (these are the fits with reduced χ^2 close to unity and fractional errors of the velocity dispersion of $\leq 3\%$).

For some objects with a strong continuum, STARLIGHT can fail to synthesize the spectrum of the host galaxy, since the flux of the lines of the host galaxy is much fainter than the AGN continuum flux. In these cases, we apply the empirical correlation $\sigma_* = \text{FWHM}[\text{OIII}]/2.35$ obtained by Nelson (2000) assuming that $\sigma_* \approx \sigma_{gas}$. The term $\text{FWHM}[\text{OIII}]$ describes the full-width-at-half-maximum of the narrow component of the $[\text{OIII}]$ emission line and is determined from a fit to the narrow lines of the $[\text{OIII}]\lambda\lambda 4959, 5007\text{\AA}$ doublet in the residual spectrum.

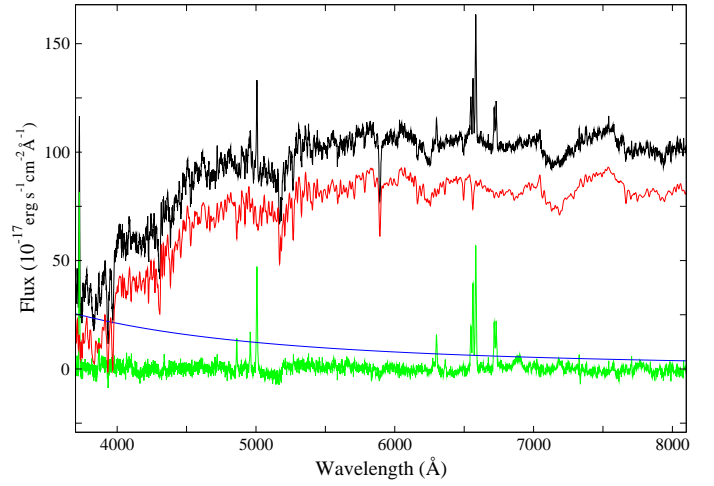


Fig. 1: STARLIGHT fit for the spectrum of the X-shaped source J1424+2637. The plot shows the observed spectrum (top black line), the modeled spectrum (second red line, displaced from observed spectrum), the AGN continuum (blue line), and the residual spectrum (bottom green line). Note that the residual spectrum contains narrow and (in some objects) broad emission lines. Properties of these lines are measured separately (see Sect. 3.2).

3.2. Emission lines

We determine the properties of the emission lines using the residual spectra obtained after subtracting the host galaxy contribution and AGN continuum from the STARLIGHT fits. The $H\beta$ and $[\text{OIII}]$ emission lines in these spectra are modeled as a combination of the narrow and broad components. We first fit three narrow Gaussian components for the oxygen $[\text{OIII}]\lambda 4959\text{\AA}$ and $[\text{OIII}]\lambda 5007\text{\AA}$ lines and for the $H\beta$ line. Three additional constraints are applied during the fitting to reduce the number of free parameters and to provide robust fits: 1) the central wavelengths of the narrow line components are set to their respective laboratory wavelengths; 2) the FWHM of the two $[\text{OIII}]$ narrow components are required to have the same value; 3) the 1:3 ratio of amplitudes of the $[\text{OIII}]\lambda 4959\text{\AA}$ and $[\text{OIII}]\lambda 5007\text{\AA}$ narrow components is fixed.

After adjusting the narrow components, broad Gaussian components are added to the $H\beta$ line, and the joint fit is further adjusted until the relative residuals are reduced to below 0.02–0.03.

3.3. Starburst histories

The STARLIGHT model for the observed spectra also yields the light fraction x_j , mass fraction M_{inj} , age τ_j , and metallicity Z_j , of the stellar populations used in the fit. We use these parameters to derive starburst histories and estimate the epochs of the most recent starbursts in the studied galaxies. We apply Gaussian smoothing to the individual starburst events (see Fig. 2) and determine the epoch of the most recent starburst episode.

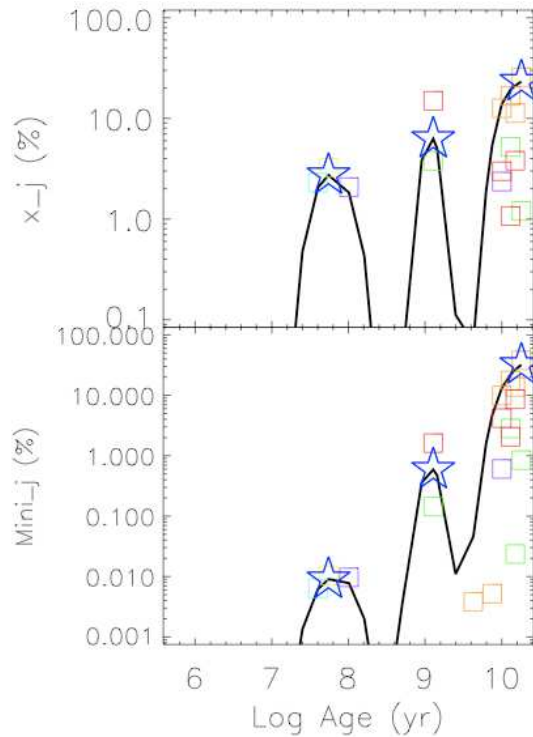


Fig. 2: STARLIGHT fits for J1327–0203: the light fraction (x_j) vs. age (top) and mass fraction $Mini_j$ vs. age (bottom) for each stellar population used. The squares correspond to stellar populations with different metallicities (in the color version: blue $0.005 Z_\odot$, purple $0.020 Z_\odot$, green $0.200 Z_\odot$, yellow $0.400 Z_\odot$, orange $1.000 Z_\odot$ and red $2.500 Z_\odot$). The solid curve represents Gaussian smoothing applied to the mass and light fraction distributions of individual starbursts. The stars indicate the identified resulting starburst episodes.

3.4. Optical continuum

Most of the X-shaped radio sources and some objects from the control sample are type II AGN (weakly beamed radio sources), for which STARLIGHT cannot provide reliable estimates of the AGN continuum flux. We estimate the rest-frame continuum flux at 5100 \AA from the SDSS photometry, with the relation (Wu & Liu 2004)

$$f_{5100\text{\AA}}[\text{Jy}] = 3631 \times 10^{-0.4g} \left[\frac{4700}{5100(1+z)} \right]^{-(g-r)/2.5 \log(6231/4770)} \quad (3)$$

where z is the redshift and the g and r fiber magnitudes are obtained from the SDSS and corrected for the Galactic extinction A_V (taken from Schlegel et al. 1998). It should be noted that the flux obtained with this method also contains a contribution from the host galaxy, but this does not introduce a strong bias in our estimates.

To assess the spectral classification of the X-shaped and control host galaxies, we measure the Ca II break of their absorption optical spectrum. This break is typically seen in the spectrum of elliptical galaxies and is described by a factor $C_{\text{CaII}} = (f_+ - f_-)/f_+$, where f_- and f_+ are the fluxes in the rest frame wavelength regions $3750\text{--}3950 \text{ \AA}$ and $4050\text{--}4250 \text{ \AA}$, respectively

(Landt et al. 2002). The Ca II break was used as an additional criterion to separate blazars from radio galaxies. Stocke et al. (1991) adopted a maximum value of $C_{\text{CaII}} = 0.25$ for BL Lacs to ensure the presence of a substantial non-thermal jet continuum in addition to the thermal spectrum of the elliptical host galaxy. This limit was later increased to $C_{\text{CaII}} < 0.4$ by other authors (Marcha et al. 1996; Plotkin et al. 2008).

Landt et al. (2010) provide the Ca II break values of 16 of the X-shaped sources studied here. For the rest of the X-shaped sources and control objects, we measure the C factor of the rest-frame optical spectra using the IRAF task `guiapps.spectool`.

3.5. Black hole masses

The measured stellar velocity dispersion, σ_* , can be connected with the mass, M_{BH} , of the central black hole through an empirical relation (Gebhardt et al. 2000; Tremaine et al. 2002):

$$M_{\text{BH}} = 1.349 \times 10^8 M_\odot \left(\frac{\sigma_*}{200 \text{ km s}^{-1}} \right)^{4.02 \pm 0.32} \quad (4)$$

. This relation is valid under the assumption that the kinematics of the stars in the bulge of the host galaxy is dominated by the gravitational potential of the central SMBH (Ferrarese & Merritt 2001).

3.6. Dynamic age of radio lobes

The dynamic age, t_a , of the high-surface-brightness (active) radio lobes is obtained from their angular size, θ_a , which is defined as the separation between the center of the radio source and the most distant contour in the FIRST image. The dynamic age is then given by θ_a/v_a , where v_a is the lobe advance speed (we adopt the commonly assumed $v_a \approx 0.1 c$; *cf.*, Tingay et al. 1998). Assuming that the fuelling of the low-surface-brightness lobes of the X-shaped sources had stopped after the high-surface ones were activated, the dynamic age of the passive lobes t_p during their active stage can be estimated as

$$t_p = \frac{\theta_p - t_a v_p}{v_a}, \quad (5)$$

where θ_p is the angular size of the low-surface brightness lobes and v_p is their expansion speed during the inactive stage. In the absence of an observational estimate for v_p , we use $v_p = 0.01 c$ in our calculation. It should be noted that reducing v_p further only has a small effect on the ages derived for the passive lobes. The total dynamic age of the X-shaped sources can then be obtained from the sum of the dynamic ages of the active and passive lobes.

4. Results

The combined results from fitting the optical spectra, black hole mass calculations, and age measurements for the radio lobes and most recent starbursts are presented in Tables 2–3.

Tables 2 and 3 list (for the X-shaped objects and the control sample, respectively) the object name based on J2000.0 coordinates (Col. 1), other common catalog names (Col. 2), stellar velocity dispersion (Col. 3), black hole mass derived from σ_* (Col. 4), optical luminosity of the AGN (Col. 5) and of the host galaxy (Col. 6), radio luminosity (Col. 7), dynamic age of the radio lobes (Col. 8), most recent starburst age (Col. 9), spectroscopic redshift (Col. 10), quality factor of the STARLIGHT fit (Col. 11), the value of Ca II break factor (Col. 12), and references for the control sources (Table 3, Col. 13). For the X-shaped sources, the total (active + passive lobe) age of the radio emission is given in brackets in Col. 8.

The control sample objects 1217+023, 2349-014, 1004+130, 3C277.1 and 3C254 are quasars with strong power-law continuum in their spectra. Estimates of σ_* for these objects are obtained from the measured width of the [OIII] line as described in Sect. 3.1. The STARLIGHT results for two X-shaped sources (J0941-0143 and J1348+4411) have provided unreliable σ_* fits (with values values of σ_* below the instrumental resolution of 70 km/s in the SDSS spectra, and quality factors $Q < 10$) and are excluded from further analysis.

4.1. Luminosity matching

Luminosity matching between the target and control samples is illustrated in Fig. 3, where the continuum luminosities derived from the SDSS magnitudes (Eq. 3) are plotted against the radio luminosities at 1.4 GHz. The entire original radio-optical luminosity range, including all sources, is called Region 0 hereafter. To provide a tighter match between the samples (at the expense of reducing the sample sizes), we define a smaller subregion or window (shown in Fig. 3) called Region 1. Region 1 ranges from $\log \lambda L_{5100\text{\AA}} \in [43.5, 44.25]$ to $\log \nu L_{1.4\text{GHz}} \in [40.25, 42.5]$ and mainly excludes the control sources with the lowest radio luminosities and highest optical luminosities because there are no X-shaped sources with such luminosities. The KS-test indicates that the statistical difference between the two samples in Region 1 is 0.9σ for the optical luminosity and 1.0σ for the radio luminosity.

4.2. Spectral classification

We base our spectral classification on color-color separation and on the Ca II break measurements in the target and control samples. All X-shaped sources analyzed have $C_{Ca II} > 0.25$, with 92% of the sources (23 out of 25) having $C_{Ca II} \approx 0.4$. These values ensure that the host galaxy of the X-shaped objects is elliptical and that it is dominated by the thermal spectrum, without any significant contribution of the non-thermal jet continuum.

For the control sample, however, the Ca II break can be determined for only 20 out of the 36 sources. Ninety percent of these sources (18 out of 20) have $C_{Ca II} > 0.25$, and 70% (14 out

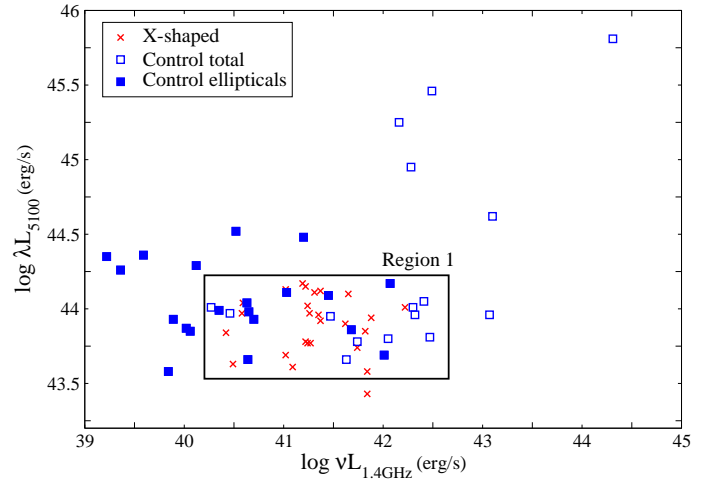


Fig. 3: Optical continuum luminosity versus radio luminosity at 1.4 GHz for X-shaped (crosses) and control sources (squares). A small sub-region (“Region 1” marked by a rectangle inside the plot) is identified to provide a tighter luminosity match between the two samples. In the further analysis, Region 1 is also subdivided into two equal bins in the radio luminosity to assess a possible luminosity dependence of the black hole mass estimates.

of 20) have $C_{Ca II} \approx 0.4$. Only 56% of the control sources therefore have a thermal spectrum that dominates the host elliptical galaxy.

The spectral classification of the X-shaped and control sources can be further refined with color-color diagrams. We use the g , r and u magnitudes obtained from SDSS to plot a $g-r$ vs $u-g$ color-color diagram (Fig. 4) for the two samples. We include in this plot only the sources with a spectrum dominated by the host galaxy (as determined from the Ca II break). According to the distribution of galaxies in the $u-g$ vs $g-r$ diagram from Strateva et al. (2001), all galaxies lying above the $u-r = 2.22$ separator line are elliptical systems. This is the case for all the X-shaped radio sources and for all the control sources for which the SDSS magnitudes are available, with only one source from each of the samples lying slightly below the $u-r = 2.22$ separator line. The X-shaped source J0049+0059 (with $u-g = 5.0$) is not plotted in Fig. 4, but it has been classified as an elliptical galaxy as well. This spectral classification agrees with the results obtained using the Ca II break feature and accordingly confirms that all X-shaped analyzed here are hosted by elliptical galaxies.

In order to better study the relation between the galactic hosts of the X-shaped and control radio sources, we will also consider a control subsample of elliptical galaxies from now on. This subsample is defined according to the galactic type obtained by the SDSS color separation described above and the Ca II break, and contains the 20 control sources for which the $C_{Ca II}$ value could be determined.

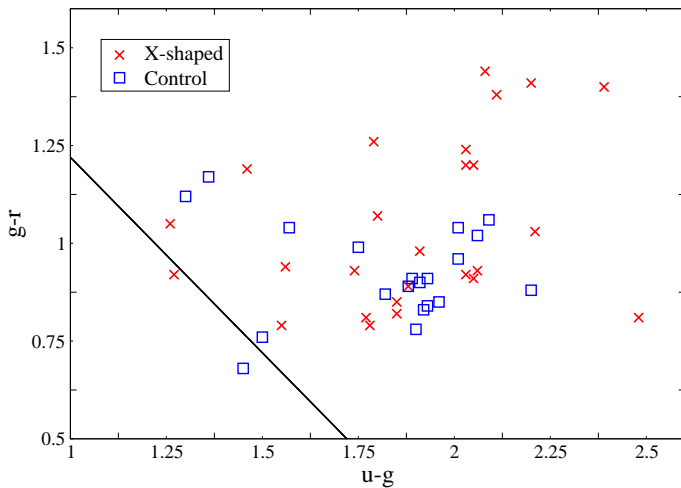


Fig. 4: Color-color diagram ($g-r$ colors versus $u-g$ colors) for X-shaped sources (cross) and control sample (square). Black line: $u - r = 2.22$ galaxy type separator from Strateva et al. (2001). Sources situated above the line are classified as ellipticals.

4.3. Black hole masses

In Table 1 we show the mean black hole mass for each sample and subsamples and for each of the regions described above (Regions 0 and 1). The ratios of the mean black hole mass defined as $r_{xc} = \langle M_{\text{BH},\text{X-shaped}} \rangle / \langle M_{\text{BH},\text{control}} \rangle$ are given as well.

A comparison of the black hole masses derived for the entire samples (objects in Region 0) yields ratios of mean BH mass ranging between 1.48 for X-shaped/control (all) to 1.13 for X-shaped/control (ellipticals).

The mass ratios derived for objects in Region 1 (tighter common range of luminosities) are higher, with the mean BH mass of the X-shaped sample being nearly twice the one derived for the whole control sample. In order to further reduce any potential effect of the source luminosity on the derived black hole mass, we calculate mass ratios in two equal-size bins in Region 1: bin 1 ranges from $\log \nu L_{1.4\text{GHz}} \in [40.25, 41.4]$ and bin 2 from $\log \nu L_{1.4\text{GHz}} \in [41.5, 42.5]$. One can see from the resulting ratios given in Table 1 that the mass ratio does not show any evolution between the bins for the whole control sample. The decrease of the mass ratio in bin 2 for the subsample of control ellipticals is owing to the small number of sources in this bin (3 sources).

The differences in the black hole masses are further illustrated in Figs. 5–6, which show histograms of the mass distributions for X-shaped and control samples in Regions 0 and 1, respectively. In both regions the X-shaped objects show a tendency to have higher black hole masses. This trend is more significant in the tighter Region 1, where 60% of the X-shaped sources have $\log M_{\text{BH}} > 8.25 M_{\odot}$ while only 25% of the whole control sample does.

The KS-test applied to the BH masses of the X-shaped and control objects indicates that the mass distributions are different

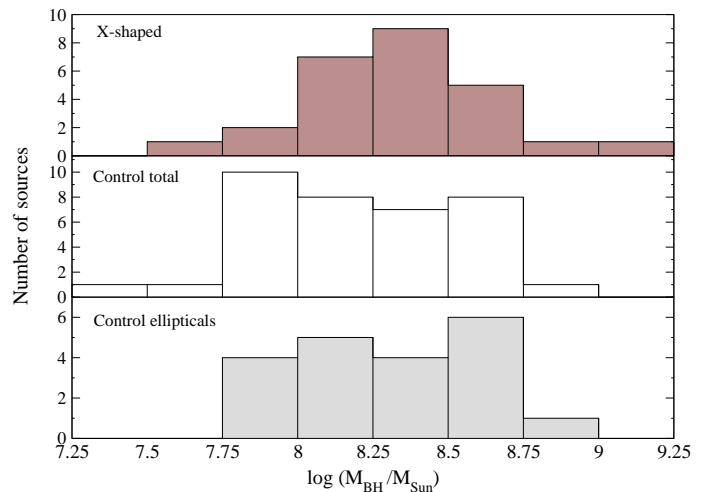


Fig. 5: Histogram of the black hole mass in Region 0 for X-shaped sources (top), control all (middle), and control ellipticals (bottom).

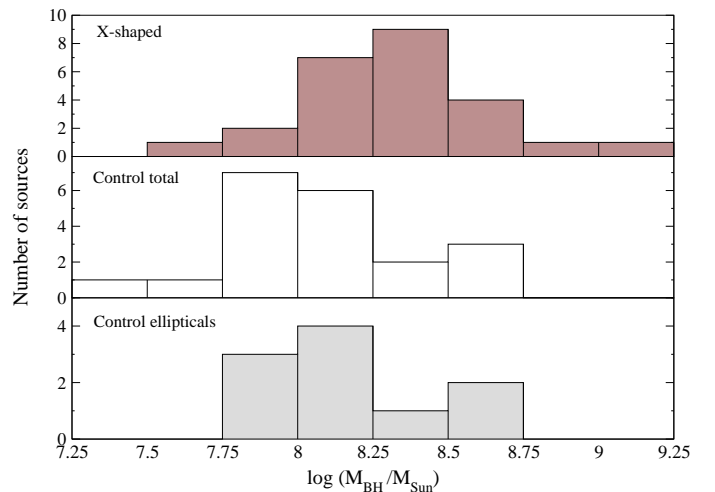


Fig. 6: Histogram of the black hole mass in Region 1 for X-shaped sources (top), control all (middle), and control ellipticals (bottom).

at a statistical significance of 1.6σ . The differences are slightly larger for objects in Region 1 (1.9σ).

The statistically larger black hole mass of the X-shaped sample implies that these objects are possibly located in galaxies that have undergone strong major activity in the past, with either one major merger event or multiple minor mergers.

4.4. Starbursts

The starburst and radio lobe ages can be used to see whether starburst activity is different in the X-shaped objects and whether it can be related to the production of radio emission in both the target and control samples.

A histogram of the ages of the most recent starburst (Fig. 7) in the objects from Region 0 shows that a sizeable fraction of objects in both samples have relatively recent starbursts, with ages

Table 1: Mean black hole masses and mass ratios

Region		X-shaped	Control (all)	Control (ellipticals)	
0	$\langle M_{\text{BH}} \rangle [M_{\odot}]$	$21.81^{+3.42}_{-2.96} \times 10^7$	$14.78^{+2.35}_{-2.03} \times 10^7$	$19.38^{+3.49}_{-2.95} \times 10^7$	
	r_{xc}		$1.48^{+0.24}_{-0.20}$	$1.13^{+0.20}_{-0.17}$	
1	$\langle M_{\text{BH}} \rangle [M_{\odot}]$	$21.03^{+3.33}_{-2.87} \times 10^7$	$10.87^{+2.34}_{-1.93} \times 10^7$	$13.98^{+3.38}_{-2.72} \times 10^7$	
	r_{xc}		$1.94^{+0.42}_{-0.34}$	$1.50^{+0.36}_{-0.29}$	
1	Bin 1	$\langle M_{\text{BH}} \rangle [M_{\odot}]$	$23.39^{+4.62}_{-3.86} \times 10^7$	$15.05^{+4.23}_{-3.30} \times 10^7$	$14.10^{+5.02}_{-3.70} \times 10^7$
		r_{xc}		$1.55^{+0.44}_{-0.34}$	$1.66^{+0.59}_{-0.44}$
	Bin 2	$\langle M_{\text{BH}} \rangle [M_{\odot}]$	$16.00^{+4.20}_{-3.33} \times 10^7$	$8.75^{+2.71}_{-2.07} \times 10^7$	$14.03^{+8.83}_{-5.42} \times 10^7$
		r_{xc}		$1.83^{+0.57}_{-0.43}$	$1.14^{+0.72}_{-0.44}$

of $10^{6.0}$ – $10^{6.5}$ years, which are possibly related to the current jet activity. The distribution of starburst ages in the X-shaped sample is much broader, with half of the objects having starbursts older than 10^8 years, while only 19% of all the control sources and 25% of the control ellipticals exhibit these starbursts. Because the largest dynamic age of the active lobes is $\sim 10^7$ years (see Tables 2 and 3, Col. 8), any starburst activity significantly older than 10^7 years is not likely to be related to the active lobes. It can be speculated that these older starbursts are related to galactic mergers themselves or to the putative coalescence of the central black holes in post-merger galaxies. The latter possibility can be viably tested by comparing the starburst ages to the dynamic ages of the active and passive lobes in the X-shaped objects.

The KS-test applied to the distributions of the most recent starburst ages gives a statistical significance of 2.3σ for the two samples being different. To account for a possible dependence of this difference on the galactic type, we apply the KS-test to the X-shaped sample and the subsample of control ellipticals. The results of the test show that the starburst ages of the X-shaped sources and the control ellipticals are still different at a statistical significance of 2.1σ .

In Fig. 8, histograms of the logarithm of the ratio of the dynamic age and most recent starburst age are plotted for the X-shaped sources and control sources of Region 0. The mean logarithmic ratios are -1.29 ± 0.23 and -0.14 ± 0.18 for the X-shaped objects and the control sample, respectively. The X-shaped sources tend to have starburst ages that are older than the dynamic ages of the radio lobes, while in both the control sample and the control subsample of ellipticals these ages are comparable. The starburst activity in X-shaped sources is therefore likely not related to the active lobes. The KS-test shows that the ratio distributions are different at a statistical significance of 2.8σ . This difference in the starburst/dynamic age ra-

tios may support the scenario in which the active lobes of the X-shaped sources are due to a possible reorientation caused by a black hole merger (Merritt & Ekers 2002) that leaves the old low-surface-brightness lobes inactive. Assuming that the low-surface-brightness lobes became inactive when the high-surface-brightness lobes were activated, the dynamic age of the passive lobes during their active stage can be determined using Eq. 5. The ratio of the total dynamic age of the active plus passive lobes to the starburst age is plotted in Fig. 8 (second panel), and it indicates that the starburst age still remains older than the total dynamic age of the lobes. This suggests that the starburst activity in X-shaped sources had occurred before the possible reorientation owing to a black hole merger, and it may have been related to the galactic merger itself.

Instead of analyzing all the X-shaped sources with optical spectra available, we can constrain the X-shaped sample to only the X-shaped radio galaxies included in the bona fide sample of Landt et al. (2010). This implies taking out 10 of the 29 X-shaped sources included in our sample, which leads to a 50% increase in the statistical errors, but does not change the obtained results. The statistical studies would be improved, on the other hand, by the addition of more X-shaped radio sources to the sample. This will be done with the availability of new optical spectra.

5. Summary

We determined and studied the black hole masses and starburst histories of 29 X-shaped radio sources to attempt to find out the most likely physical scenario for the formation of their peculiar morphology. We compared the black hole masses and properties of the starburst activity derived for this sample with those obtained for a control sample of 36 galaxies with common optical and radio luminosities. The main results of this study can be summarized as follows.

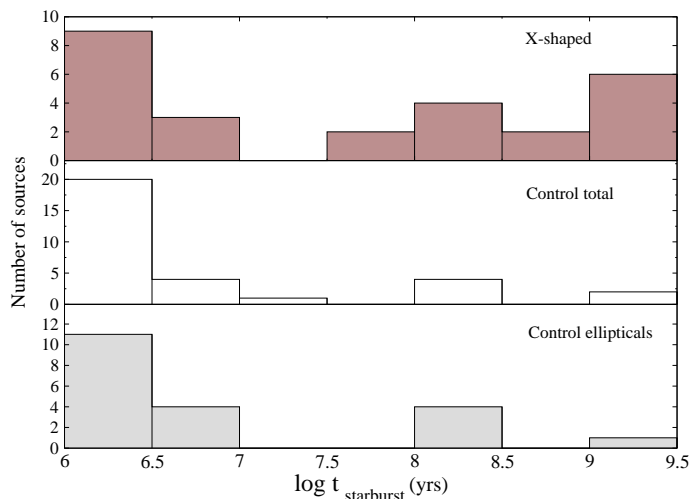


Fig. 7: Histogram of the most recent starburst for X-shaped sources (top), control all (middle), and control ellipticals (bottom).

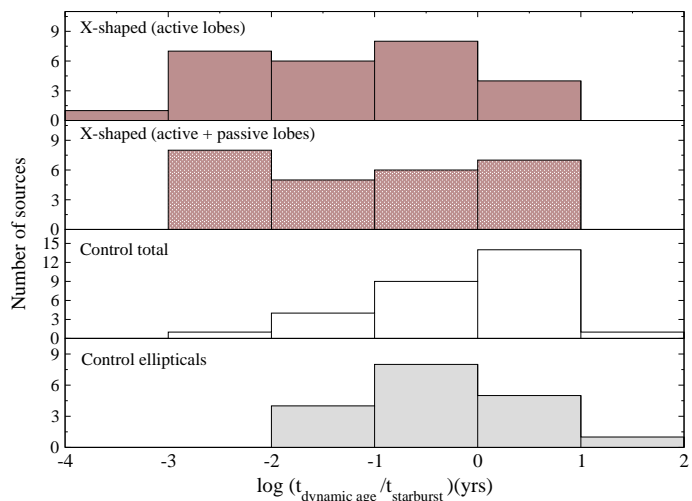


Fig. 8: Logarithmic ratios of the dynamic age of the radio emission to the age of the most recent starburst for Region 0. The top row presents the ages of active lobes in X-shaped objects, while the second row shows the sum of the ages of the active and passive lobes. The two bottom rows show distributions of the age ratios in the control sample (third row) and the subsample of control ellipticals (fourth row).

The Ca II break feature of the absorption spectrum and the optical colors obtained from the SDSS u, g, r photometry data indicate that all X-shaped radio sources studied in this paper are hosted by elliptical galaxies. In the hierarchical galaxy-formation model, today's galaxies are the product of frequent galaxy merging, triggering starburst and active galactic nuclei activity and possibly forming supermassive binary black hole systems (Frenk et al. 1988; Hutchings & Campbell 1983; Sanders et al. 1988; Hopkins et al. 2006). There appears to be supporting evidence that elliptical galaxies have formed from mergers in a hierarchical way (Toomre & Toomre 1972; Efsthathiou & Silk 1983). Therefore the trend for X-shaped ra-

dio sources to reside in elliptical galaxies suggests that their X-shaped morphology could be related to the galaxy merger scenario.

The mean black hole mass of the objects in the X-shaped sample is found to be statistically higher than in the control sample. This result holds for the entire range of the radio and optical luminosities as well as for smaller subranges and for exact galactic type-matching between the two samples.

The statistically higher black hole masses obtained for the X-shaped objects suggest that their peculiar radio morphology can indeed result from a reorientation of the jet axis owing to black hole coalescence or from the presence of two active central engines in the nuclear region.

A comparison of the starburst ages and dynamic ages of the radio lobes reveals that the most recent starburst activity in X-shaped sources is older than in the control sample and that X-shaped radio sources had their most recent starburst before their active lobes were formed. These results lend further support to the scenario in which the high-surface-brightness lobes might have become active due to reorientation caused by a black hole coalescence, while the peak of starburst activity could be connected to the galactic merger itself.

Another scenario proposed to explain the X-shaped morphology in X-shaped radio galaxies employs the backflow emission of the active lobes into the wings. This model is based on the presence of pressure gradients in the confining medium of the jet and does not seem to be able to explain the results we obtained. Although our findings argue in favor of the merger scenario, they do not rule out entirely the backflow model. It should be further noted that it is quite possible that some X-shaped sources may indeed have undergone a merger, while in others the peculiar shape might be caused by a backflow of the active jets.

Acknowledgments

The authors are grateful to the anonymous referee for insightful comments and suggestions. The authors thank C.C. Cheung for providing optical spectroscopy data and M. Karouzos for his valuable assistance. M. Mezcuca was supported for this research through a stipend from the International Max Planck Research School (IMPRS) for Radio and Infrared Astronomy at the Universities of Bonn and Cologne. This work was supported by the CONACYT research grant 54480 (México). The STARLIGHT project is supported by the Brazilian agencies CNPq, CAPES and FAPESP and by the France-Brazil CAPES/Cofecub program.

References

- Adelman-McCarthy, J. K., et al. 2008, *ApJS*, 175, 297
- Antonucci, R. R. J. 1985, *ApJS*, 59, 499
- Asari, N. V., Cid Fernandes, R., Stasińska, G., Torres-Papaqui, J. P., Mateus, A., Sodré, L., Schoenell, W., Gomes, J. M. . 2007, *MNRAS*, 381, 263

- Becker, R. H., White, R. L., & Helfand, D. J. 1995, *ApJ*, 450, 559
- Blecha, L., Cox, T. J., Loeb, A., & Hernquist, L. 2010, arXiv:1009.4940
- Bruzual, G., & Charlot, S. 2003, *MNRAS*, 344, 1000
- Capetti, A., Zamfir, S., Rossi, P., Bodo, G., Zanni, C., & Massaglia, S. 2002, *A&A*, 394, 39
- Cardelli, J. A., Clayton, G. C., & Mathis, J. S. 1989, *ApJ*, 345, 245
- Cheung, C. C. 2007, *AJ*, 133, 2097
- Cheung, C. C., Healey, S. E., Landt, H., Kleijn, G. V., & Jordán, A. 2009, *ApJS*, 181, 548
- Cid Fernandes, R., Gu, Q., Melnick, J., Terlevich, E., Terlevich, R., Kunth, D., Rodrigues Lacerda, R., & Joguet, B. 2004, *MNRAS*, 355, 273
- Cid Fernandes, R., Mateus, A., Sodré, L., Stasińska, G., & Gomes, J. M. 2005, *MNRAS*, 358, 363
- Cid Fernandes, R., Asari, N. V., Sodré, L., Stasińska, G., Mateus, A., Torres-Papaqui, J. P., & Schoenell, W. 2007, *MNRAS*, 375, L16
- Dennett-Thorpe, J., Scheuer, P. A. G., Laing, R. A., Bridle, A. H., Pooley, G. G., & Reich, W. 2002, *MNRAS*, 330, 609
- Dokuchaev, V. I. 1991, *MNRAS*, 251, 564
- Efstathiou, G., & Silk, J. 1983, *Fund. Cosmic Phys.*, 9, 1
- Frenk, C. S., White, S. D. M., Davis, M., & Efstathiou, G. 1988, *ApJ*, 327, 507
- Gebhardt, K., et al. 2000, *ApJ*, 539, L13
- Gergely, L. Á., & Biermann, P. L. 2009, *ApJ*, 697, 1621
- González-Serrano, J. I., & Carballo, R. 2000, *A&AS*, 142, 353
- Gopal-Krishna, Biermann, P. L., & Wiita, P. J. 2003, *ApJ*, 594, L103
- Gopal-Krishna, Biermann, P. L., Gergely, L. Á., & Wiita, P. J. 2010, arXiv:1008.0789
- Hodges-Kluck, E. J., Reynolds, C. S., Cheung, C. C., & Miller, M. C. 2010, *ApJ*, 710, 1205
- Hodges-Kluck, E. J., Reynolds, C. S., Miller, M. C., & Cheung, C. C. 2010, *ApJ*, 717, L37
- Hopkins, P. F., Hernquist, L., Cox, T. J., Di Matteo, T., Robertson, B., & Springel, V. 2006, *ApJS*, 163, 1
- Hutchings, J. B., & Campbell, B. 1983, *Nature*, 303, 584
- Hutchings, J. B., Frenette, D., Hanisch, R., Mo, J., Dumont, P. J., Redding, D. C., & Neff, S. G. 2002, *AJ*, 123, 2936
- Kaspi, S., Smith, P. S., Netzer, H., Maoz, D., Jannuzi, B. T., & Giveon, U. 2000, *ApJ*, 533, 631
- Kaspi, S., Maoz, D., Netzer, H., Peterson, B. M., Vestergaard, M., & Jannuzi, B. T. 2005, *ApJ*, 629, 61
- Lal, D. V., & Rao, A. P. 2005, *Astronomical Society of the Pacific Conference Series*, 345, 289
- Lal, D. V., & Rao, A. P. 2007, *MNRAS*, 374, 1085
- Landt, H., Padovani, P., & Giommi, P. 2002, *MNRAS*, 336, 945
- Landt, H., Cheung, C. C., & Healey, S. E. 2010, *MNRAS*, 408, 1103
- Leahy, J. P., & Williams, A. G. 1984, *MNRAS*, 210, 929
- Leon-Tavares, J., Valtaoja, E., Chavushyan, V. H., Tornikoski, M., Anorve, C., Nieppola, E., & Lahteenmaki, A. 2010, *MNRAS*(in press), arXiv:1009.6195
- Lobanov, A. P. 2008, *Memorie della Societa Astronomica Italiana*, 79, 1306
- Mack, K.-H., Gregorini, L., Parma, P., & Klein, U. 1994, *A&AS*, 103, 157
- Mateus, A., Sodre, L., Cid Fernandes, R., Stasinska, G., Schoenell, W., & Gomes, J. M. 2006, *MNRAS*, 370, 721
- Marcha, M. J. M., Browne, I. W. A., Impey, C. D., & Smith, P. S. 1996, *MNRAS*, 281, 425
- Marchesini, D., Celotti, A., & Ferrarese, L. 2004, *MNRAS*, 351, 733
- Merritt, D., & Ferrarese, L. 2001, *ApJ*, 547, 140
- Merritt, D., & Ekers, R. D. 2002, *Science*, 297, 1310
- Nelson, C. H. 2000, *ApJ*, 544, L91
- Parma, P., Ekers, R. D., & Fanti, R. 1985, *A&AS*, 59, 511
- Plotkin, R. M., Anderson, S. F., Hall, P. B., Margon, B., Voges, W., Schneider, D. P., Stinson, G., & York, D. G. 2008, *AJ*, 135, 2453
- Rees, M. J. 1978, *Nature*, 275, 516
- Sanders, D. B., Soifer, B. T., Elias, J. H., Neugebauer, G., & Matthews, K. 1988, *ApJ*, 328, L35
- Schlegel, D. J., Finkbeiner, D. P., & Davis, M. 1998, *ApJ*, 500, 525
- Stocke, J. T., Morris, S. L., Gioia, I. M., Maccacaro, T., Schild, R., Wolter, A., Fleming, T. A., & Henry, J. P. 1991, *ApJS*, 76, 813
- Strateva, I., et al. 2001, *AJ*, 122, 1861
- Tingay, S. J., et al. 1998, *AJ*, 115, 960
- Toomre, A., & Toomre, J. 1972, *ApJ*, 178, 623
- Tremaine, S., et al. 2002, *ApJ*, 574, 740
- de Vries, W. H., Becker, R. H., & White, R. L. 2006, *AJ*, 131, 666
- Wang, T.-G., Zhou, H.-Y., & Dong, X.-B. 2003, *AJ*, 126, 113
- Wu, X.-B., & Liu, F. K. 2004, *ApJ*, 614, 91

Table 2: X-shaped objects

Name		σ_*	$\log M_{\text{BH}}$	$\log \lambda L_{\text{opt}}^{\text{agn}}$	$\log \lambda L_{\text{opt}}^{\text{gal}}$	$\log \nu L_{\text{rad}}$	$\log t_a$ ($\log t_p$)	$\log t_{\text{sb}}$	z	Q	C_{CaII}
J2000	Other	[km/s]	[M_{\odot}]	[erg/s]	[erg/s]	[erg/s]	[yr]	[yr]	(10)	(11)	(12)
(1)	(2)	(3)	(4)	(5)	(6)	(7)	(8)	(9)			
J0001-0033		277.32 ± 4.55	8.70 ± 0.03	- <i>b</i>	43.77	41.27	6.37 (6.60)	6.50	0.247	83.94	0.43 ^f
J0049+0059		282.23 ± 9.64	8.73 ± 0.06	- <i>b</i>	43.43	41.84	6.68 (6.83)	9.20	0.304	31.07	
J0808+2409	3C192	209.94 ± 7.97	8.21 ± 0.07	- <i>b</i>	43.85	41.82	6.52 (6.71)	6.70	0.060	41.46	0.36
J0813+4347		251.25 ± 5.79	8.53 ± 0.04	- <i>b</i>	44.11	41.31	6.29 (6.49)	9.10	0.128	44.69	0.45 ^f
J0831+3219	4C+32.25	194.80 ± 6.21	8.08 ± 0.06	42.42 ± 0.14	43.97	41.26	6.69 (6.85)	6.50	0.051	59.44	0.44 ^f
J0838+3253		241.60 ± 11.43	8.46 ± 0.08	- <i>b</i>	43.92	41.37	6.59 (6.76)	8.50	0.213	28.77	0.42
J0859-0433		250.37 ± 12.90	8.52 ± 0.09	42.33 ± 2.65	- <i>c</i>	42.13	6.08 (6.65)	8.00	0.356	24.55	
J0924+4233		231.16 ± 15.72	8.38 ± 0.12	- <i>b</i> -	43.58	41.84	6.54 (6.77)	9.00	0.227	15.96	0.42 ^f
J0941-0143		154.92 ± 20.61	7.68 ± 0.23	42.48 ± 5.15	43.19	42.84	6.14 (6.64)	7.00	0.384	4.92 ^e	
J0941+3944	3C223.1	196.90 ± 9.14	8.10 ± 0.08	42.30 ± 0.87	43.94	41.88	6.44 (6.78)	9.11	0.107	35.30	0.38 ^f
J1005+1154		272.88 ± 6.46	8.67 ± 0.04	- <i>b</i> -	44.12	41.37	6.43 (6.67)	9.10	0.166	66.08	0.48 ^f
J1020+4831	4C+48.29	194.30 ± 7.94	8.08 ± 0.07	42.28 ± 0.19	43.78	41.22	6.72 (7.02)	8.46	0.053	38.82	0.44 ^f
J1040+5056		211.57 ± 15.88	8.23 ± 0.13	- <i>b</i> -	43.77	41.24	6.44 (6.65)	9.20	0.154	20.74	0.42
J1043+3131		195.27 ± 8.24	8.09 ± 0.07	41.15 ± 1.15	43.63	40.49	5.80 (6.09)	6.80	0.036	32.66	0.41
J1101+1640	1059+169	220.98 ± 6.42	8.30 ± 0.05	41.01 ± 5.18	43.69	41.02	6.62 (6.98)	6.00	0.069	60.03	0.45 ^f
J1111+4050		254.75 ± 4.96	8.55 ± 0.03	- <i>b</i> -	44.17	41.19	6.16 (6.43)	6.50	0.074	74.31	0.43
J1130+0058	4C+01.30	151.86 ± 6.78	7.65 ± 0.08	43.12 ± 0.15	44.10	41.65	6.24 (6.61)	9.40	0.132	24.88	0.26 ^f
J1140+1057		196.37 ± 7.80	8.10 ± 0.07	40.51 ± 20.11	43.61	41.09	6.28 (6.51)	6.00	0.081	40.99	0.41 ^f
J1207+3352		181.28 ± 3.79	7.96 ± 0.04	41.85 ± 0.84	44.13	41.02	6.19 (6.44)	6.00	0.079	51.36	0.28 ^f
J1210-0341		221.29 ± 9.90	8.30 ± 0.08	42.14 ± 2.94	43.90	41.62	5.97 (6.56)	8.70	0.178	33.61	0.40 ^f
J1210+1121		223.51 ± 9.41	8.32 ± 0.07	- <i>b</i> -	43.96	41.35	6.66 (6.78)	7.60	0.196	33.55	0.42
J1327-0203		237.30 ± 9.27	8.43 ± 0.07	- <i>b</i> -	44.01	42.22	6.39 (6.65)	7.70	0.183	38.98	0.48 ^f
J1330-0206		219.35 ± 7.72	8.29 ± 0.06	- <i>b</i> -	44.04	40.59	6.35 (6.61)	7.00	0.087	42.40	0.40
J1339-0016		323.77 ± 4.55	8.97 ± 0.02	- <i>b</i> -	44.15	41.22	6.55 (6.81)	8.50	0.145	88.09	0.44
J1348+4411		108.42 ± 27.71	7.05 ± 0.45	41.67 ± 10.43	43.28	41.63	5.87 (6.53)	6.90	0.267	2.95 ^e	
J1424+2637		174.99 ± 6.53	7.90 ± 0.07	40.48 ± 6.37	43.97	40.58	6.13 (6.37)	6.50	0.037	45.36	0.40
J1444+4147		226.06 ± 9.35	8.34 ± 0.07	- <i>b</i> -	43.74	41.74	6.60 (6.80)	8.50	0.188	35.89	0.44 ^f
J1455+3237		224.17 ± 5.52	8.33 ± 0.04	41.57 ± 1.78	43.84	40.42	6.10 (6.31)	6.50	0.084	68.39	0.39
J1614+2817		344.13 ± 6.21	9.08 ± 0.03	41.32 ± 2.65	44.02	41.24	5.59 (6.22)	6.00	0.108	25.85	0.42 ^f

Column designation: (1) – object name based on J2000.0 coordinates; (2) – other common catalog names; (3) – stellar velocity dispersion obtained from STARLIGHT; (4) – black hole mass obtained from σ_* ; (5) – 5100 Å continuum luminosity from STARLIGHT; (6) – 5100 Å continuum luminosity from SDSS photometry; (7) – 1.4 GHz radio luminosity; (8) – dynamic age of the active (active+passive) lobes; (9) – age of the most recent starburst; (10) – spectroscopic redshift from SDSS; (11) – quality factor; (12) value of Ca II break factor. **Notes:** *a* – velocity dispersion obtained using the correlation $\sigma_* = \text{FWHM} [\text{OIII}]/2.35$; *b* – STARLIGHT could not fit the continuum luminosity; *c* – no SDSS photometry available; *d* – no STARLIGHT fit; *e* – low fidelity of the STARLIGHT fit; *f* – values of Ca II break from Landt et al. (2010)

Table 3: Control sample

J2000 (1)	Name		σ_*	$\log M_{\text{BH}}$	$\log \lambda L_{\text{opt}}^{\text{agn}}$	$\log \lambda L_{\text{opt}}^{\text{gal}}$	$\log \nu L_{\text{rad}}$	$\log t_a$	$\log t_{\text{sb}}$	z	Q	C_{CaII}	Ref.
	Other (2)	[km/s] (3)	$[M_{\odot}]$ (4)	[erg/s] (5)	[erg/s] (6)	[erg/s] (7)	[yr] (8)	[yr] (9)	(10)	(11)	(12)	(13)	
J0758+3747	0755+37	251.55 ± 4.63	8.53 ± 0.03	41.58 ± 0.09	44.48	41.20	6.16	6.00	0.043	85.50	0.36	M04	
J0803+2440	B2 0800+24	186.04 ± 0.13	8.00 ± 0.06	- <i>b</i>	43.85	40.06	6.42	6.50	0.043	55.56	0.42	G00	
J0821+4702	3C197.1	144.35 ± 9.53	7.56 ± 0.12	42.46 ± 0.05	43.80	42.05	6.11	6.00	0.128	17.33	-	M04	
J0822+0557	3C198	164.35 ± 5.76	7.79 ± 0.06	42.46 ± 0.02	43.66	41.63	6.43	6.00	0.081	51.31	-	M04	
J0846+3126	B2 0843+31	183.02 ± 0.14	7.98 ± 0.07	- <i>b</i>	43.58	39.84	6.98	7.00	0.067	43.13	0.41	G00	
J0921+4538	3C219	188.98 ± 8.49	8.03 ± 0.08	42.52 ± 0.07	43.96	43.07	6.94	6.00	0.174	21.14	-	M04	
J0925+3627	4C36.14	256.37 ± 0.35	8.56 ± 0.04	- <i>b</i>	44.26	39.36	6.60	7.00	0.112	68.51	0.43	G00	
J0939+3553	3C223	181.42 ± 8.26	7.96 ± 0.08	42.45 ± 0.06	43.81	42.47	7.06	9.40	0.137	24.50	-	M04	
J0941+5751	J0941+5751	189.32 ± 7.83	8.03 ± 0.07	- <i>b</i>	43.97	40.46	6.43	6.00	0.159	29.56	-	V06	
J0947+0725	3C227	112.51 ± 3.35	7.13 ± 0.05	43.63 ± 0.00	43.95	41.47	6.78	6.00	0.086	24.43	-	M04	
J1006+2554	B2 1003+26	240.82 ± 0.40	8.45 ± 0.06	- <i>b</i>	44.52	40.52	7.17	9.11	0.117	38.18	0.44	G00	
J1006+3454	3C236	247.41 ± 7.26	8.5 ± 0.05	- <i>b</i>	44.17	42.07	7.74	6.50	0.101	54.96	0.33	M04	
J1007+1248	1004+130	167.82 ^a ± 1.05	7.77 ± 0.01	- <i>b</i>	45.46	42.49	6.89	- <i>d</i>	0.241	- <i>d</i>	-	M04	
J1031+5225	J1031+5225	204.85 ± 11.06	8.17 ± 0.09	42.34 ± 0.10	43.69	42.01	6.42	6.00	0.166	22.09	0.28	V06	
J1040+2957	4C30.19	161.97 ± 0.06	7.76 ± 0.04	- <i>b</i>	44.11	41.03	- <i>c</i>	8.01	0.091	61.46	0.18	G00	
J1055+5202	J1055+5202	162.90 ± 12.40	7.77 ± 0.13	42.61 ± 0.11	43.78	41.74	6.46	6.00	0.187	12.12	-	V06	
J1105+3009	B2 1102+30A	262.26 ± 0.35	8.60 ± 0.04	41.14 ± 6.59	44.35	39.22	6.35	6.50	0.072	74.22	0.43	G00	
J1114+4037	3C254	234.20 ^a ± 3.29	8.35 ± 0.03	- <i>b</i>	45.81	44.31	1.55	- <i>d</i>	0.736	- <i>d</i>	-	M04	
J1154+0238	J1154+0238	169.59 ± 11.91	7.84 ± 0.12	- <i>b</i>	43.66	40.64	6.46	6.70	0.211	18.78	0.31	V06	
J1219+0549	3C270	269.46 ± 3.72	8.65 ± 0.02	- <i>b</i>	44.04	40.63	6.12	7.00	0.007	84.46	0.41	M04	
J1220+0203	1217+023	174.94 ^a ± 1.72	7.84 ± 0.02	- <i>b</i>	45.25	42.16	6.84	- <i>d</i>	0.240	- <i>d</i>	-	M04	
J1252+5634	3C277.1	235.90 ^a ± 0.57	8.37 ± 0.00	- <i>b</i>	44.62	43.10	5.04	- <i>d</i>	0.320	- <i>d</i>	-	M04	
J1259+2757	NGC4874	251.47 ± 0.32	8.53 ± 0.04	- <i>b</i>	44.36	39.59	6.30	6.00	0.024	57.54	0.42	G00	
J1319+2938	4C29.47	198.73 ± 0.17	8.12 ± 0.06	- <i>b</i>	44.09	41.45	6.35	8.01	0.073	53.97	0.39	G00	
J1321+4235	3C285	162.58 ± 9.46	7.77 ± 0.10	- <i>b</i>	43.86	41.68	6.6	6.00	0.079	26.37	0.24	M04	
J1332+0200	3C287.1	246.02 ± 7.86	8.49 ± 0.06	43.24 ± 0.04	44.01	40.27	6.82	6.00	0.216	32.12	-	M04	
J1341+5344	J1341+5344	225.84 ± 7.07	8.34 ± 0.05	- <i>b</i>	43.87	40.02	6.55	6.00	0.141	42.80	0.31	V06	
J1350+2816	B2 1347+28	209.58 ± 0.23	8.21 ± 0.06	- <i>b</i>	43.98	40.65	6.34	8.01	0.072	46.69	0.41	G00	
J1430+5201	3C303	167.41 ± 9.77	7.82 ± 0.10	43.22 ± 0.01	43.96	42.32	6.28	7.20	0.141	16.86	-	M04	
J1512+0203	J1512+0203	194.50 ± 10.45	8.08 ± 0.09	42.79 ± 0.09	44.01	42.30	6.52	6.00	0.219	25.33	-	V06	
J1529+3042	1527+30	322.89 ± 7.49	8.97 ± 0.01	- <i>b</i>	44.29	40.12	6.38	8.20	0.114	64.60	0.46	G00	
J1559+2556	B2 1557+26	223.51 ± 0.24	8.32 ± 0.05	41.09 ± 15.68	43.93	39.89	- <i>c</i>	6.00	0.045	54.67	0.4	G00	
J1611+3103	B2 1609+31	199.34 ± 0.23	8.12 ± 0.08	- <i>b</i>	43.93	40.70	5.74	6.00	0.095	31.15	0.42	G00	
J1615+2726	1613+27	221.13 ± 6.13	8.31 ± 0.05	41.11 ± 0.40	43.99	40.35	5.89	6.00	0.065	58.17	0.42	M04	
J1617+3222	3C332	172.37 ± 3.80	8.64 ± 0.01	40.90 ± 4.45	44.05	42.41	6.62	6.00	0.151	33.13	-	M04	
J2351-0109	2349-014	201.97 ^a ± 2.12	8.72 ± 0.01	- <i>b</i>	44.95	42.28	6.06	- <i>d</i>	0.174	- <i>d</i>	-	M04	

Column designation: (1) – object name based on J2000.0 coordinates; (2) – other common catalog names; (3) – stellar velocity dispersion obtained from STARLIGHT; (4) – black hole mass obtained from σ_* ; (5) – 5100 Å continuum luminosity from STARLIGHT; (6) – 5100 Å continuum luminosity from SDSS photometry; (7) – 1.4 GHz radio luminosity; (8) – dynamic age of the active lobes; (9) – age of the most recent starburst; (10) – spectroscopic redshift from SDSS; (11) – quality factor; (12) value of Ca II break factor; (13) – Original references. **Notes:** *a* – velocity dispersion obtained using the correlation $\sigma_* = \text{FWHM}[\text{OIII}]/2.35$; *b* – STARLIGHT could not fit the continuum luminosity; *c* – not available; *d* – no STARLIGHT fit. **REFERENCES.**– (G00) González-Serrano & Carballo (2000); (M04) Marchesini et al. (2004); (V06) de Vries et al. (2006).